Deep roots for mid-ocean ridge volcanoes revealed by plagioclase-hosted melt inclusions

Emma N. Bennett[a], Frances E. Jenner[b], Marc-Alban Millet[a], Katharine V. Cashman[c] and C. Johan Lissenberg[a]

[a] School of Earth and Ocean Sciences, Cardiff University, Park Place, Cardiff CF10 3AT, UK

[b]School of Environment, Earth and Ecosystem Sciences, The Open University, Walton Hall, Milton Keynes MK7 6AA, UK.

[c]School of Earth Sciences, University of Bristol, Wills Memorial Building, Bristol BS8 1RJ, UK

The global mid-ocean ridge system is the most significant magmatic system on our planet and is the site of 75% of Earth volcanism[1]. The vertical extent of mid-ocean ridge magmatic systems has been considered to be restricted: even at the ultraslow-spreading Gakkel Ridge, where the lithosphere is thickest, crystallisation depths of magmas feeding eruptions are thought to be <9 km[2]. These depths have been determined using the volatile contents of melt inclusions, which are small volumes of magma that become trapped within crystallising minerals. In studies of basaltic magmatic systems, olivine is the mineral of choice for this approach[2–6]. However, pressures derived from olivine-hosted melt inclusions are at odds with pressures derived from basalt major element barometers[7] and geophysical measurements of lithospheric thickness[8]. Here, we present a comparative study of olivine- and plagioclase- hosted melt inclusions from the ultraslow-spreading Gakkel mid-ocean ridge (Arctic Ocean). We show that the volatile contents of (complexly zoned) plagioclase-hosted melt inclusions correspond to significantly higher crystallisation pressures (mean 270 MPa) than (simply zoned) olivine-hosted melt inclusions (mean 145 MPa). The highest recorded pressure we find equates to 16.4 km depth below the seafloor. These higher depths are consistent with both the thickness of the Gakkel

Ridge lithosphere and pressures reconstructed from glass compositions. Contrary to previous studies using olivine-hosted melt inclusions, our results demonstrate that mid-ocean ridge volcanoes may have magmatic roots deep in the lithospheric mantle, at least at ultraslow spreading ridges.

Direct constraints on the depth of crystallisation beneath mid-ocean ridge volcanoes, the most productive magmatic system on Earth, come from melt inclusions[2–7]. Crystallisation pressures determined from melt inclusion volatile contents typically correspond to the depth of seismically imaged melt lenses[5] and reveal that much of the crystallisation is restricted to crustal depths[4–6] (nominally 6 km), with limited crystallisation up to 9.9 km[6]. These pressures suggest that mid-ocean ridge volcanoes have shallow magmatic roots that are largely restricted to the lower oceanic crust, with limited sourcing of eruptions from the lithospheric mantle[5,6,9,10]. However, lithospheric thickness[8] and crystallisation pressures determined from basalt major element barometers[7] are greater than that suggested by olivine-hosted melt inclusions, particularly at ultraslow-spreading ridges. A case in point is the Gakkel Ridge, where melt inclusion vapour saturation pressures (40-309 MPa or 0-9 km below seafloor[2,3]) are substantially less than the proposed lithospheric thickness (≤35 km[8]) and petrological estimates of crystallisation pressures from basalt major elements (≤600 MPa or ~20 km)[7]. These contradictory records raise questions about the true vertical extent of mid-ocean ridge magmatic systems.

Melt inclusions are key tools to address this issue. Whilst major element systematics of basalts may also be used to constrain crystallisation pressures, the values integrate what is essentially a polybaric crystallisation path. Furthermore, these pressures are based on the assumption that no melt-crystal reactions occur in the magmatic plumbing system – a process for which there is abundant evidence[11]. Basalt compositions, therefore, are unlikely to record unique depths. In contrast, melt inclusions have the potential to record an

accurate, fine-scale, polybaric pressure record if they are trapped within host minerals at different depths during transport through the magmatic plumbing system. Olivine-hosted melt inclusions are often preferred because: (1) olivine is a primitive, early-formed mineral[12], and hence should, in principle, track the earliest stages of magmatic differentiation; and (2) olivine is viewed as a tighter "vessel" compared to plagioclase, which possesses cleavage planes along which volatiles may escape[13,14]. However, the low vapour saturation pressures recorded by olivine-hosted melt inclusions, not only from mid-ocean ridges but also from a range of low-H_2O basaltic settings including ocean islands, continental rifts and arcs, poses a significant question as to their ability to capture the full depth range of the magmatic plumbing systems from which they are sourced[15].

Here, we suggest that plagioclase may preserve a more complete record of crystallisation pressures than olivine. Importantly, plagioclase crystals typically show more complex compositional zoning and variable crystal habits than olivine. Whilst slower major element diffusion in plagioclase[16] compared to that in olivine[17] may account for the differential preservation of zoning, the sheer variety of zoning patterns and habits raises the possibility that plagioclase may preserve a more extensive part of the crystallisation history than olivine. Plagioclase is frequently more abundant in volcanic rocks (including mid-ocean ridge basalts) compared to olivine[18]. Hence, if plagioclase-hosted melt inclusions can provide a reliable record of pressures, this would improve reconstructions of magmatic plumbing systems.

We have combined detailed textural analysis of host olivine and plagioclase crystals with measurements of the volatile (H_2O and CO_2) content of 30 olivine-hosted and 75 plagioclase-hosted melt inclusions from the Gakkel Ridge to compare their respective records of crystallisation. The 15 samples studied were retrieved from nine locations that cover the full extent of the Gakkel Ridge (Extended Data Figure 1). These data are

supplemented by trace element data on 93 melt inclusions, and by existing data from olivine-hosted melt inclusions from this region[2,3].

The contrasting textural complexity of olivine and plagioclase is illustrated in Fig. 1 and Extended Data Figure 2. Whilst both phases exhibit a range of crystal habits (Fig.1), plagioclase shows more evidence of resorption (Fig.1a compared to d,f,h,i) and more complex zoning, although both phases may also lack zoning (Fig. 1b,c and h). Zoning patterns in plagioclase include, but are not restricted to, reverse zoning (Fig. 1e,g), concentric zoning punctuated by undulose resorption interfaces (Fig. 1f) and complex combinations of patchy and concentric zoning (Fig. 1i). Complex zoning patterns (Fig. 1d,e,f,i) and large amoeboid melt inclusions interpreted as the product of resorption (Fig. 1h,i), indicate that plagioclase crystals have experienced protracted growth (±resorption) histories within open magmatic systems.

Olivine-hosted melt inclusions are found in host crystals with both skeletal (37%; Fig.1 b) and non-skeletal morphologies (63%; Fig. 1c). In euhedral and subhedral olivine, inclusions are randomly distributed (Fig. 1c) whilst those in skeletal olivine are found in hour-glass arrangements or located close to the host margins (Fig. 1b). The inclusions in olivine are not associated with observable zonation, although whilst not mapped, trace elements (i.e., P) may preserve zoning[19]. For the most part, melt inclusions in plagioclase are either randomly distributed throughout the host crystal (Fig. 1h,i) or restricted to cores (Fig. 1g), while only 4% of those analysed are directly associated with resorption interfaces (Fig. 1f).

The Gakkel Ridge volatile data are presented in Figure 2, along with other olivine-hosted melt inclusion data for which saturation pressures have been calculated. H_2O concentrations of both olivine- and plagioclase-hosted melt inclusions are similar and range from 0.12-0.56 wt.% H_2O, although plagioclase-hosted melt inclusions record a larger range of CO_2 (282-2857 ppm) than olivine-hosted melt inclusions (94-1984 ppm). Furthermore, plagioclase-

hosted melt inclusions have significantly higher median CO_2 contents (1668 ppm) compared to olivine-hosted melt inclusions (637 ppm). There is no correlation between melt inclusion size (Extended Data Figure 3) or location (Fig. 3b) with CO_2. Two lines of evidence indicate that the Gakkel melt inclusions, including the CO_2-rich plagioclase-hosted inclusions, are CO_2 saturated. First, inclusions define a positive Mg#-CO_2 correlation (Fig. 3a) indicative of concomitant crystallisation (decreasing Mg#) and degassing. Second, the inclusions fall on the global MORB array for CO_2/Ba. The maximum CO_2/Ba of 145 is consistent with the proposed CO_2/Ba ratio of the mantle (~140; ref. 24), the remaining inclusions have lower ratios consistent with variable degrees of degassing (Fig. 3c,d).

The CO_2 record of Gakkel plagioclase-hosted melt inclusions is unlike that of olivine from either the Gakkel Ridge or from mid-ocean ridges elsewhere, being offset to higher values (Fig. 2). The volatile contents of Gakkel Ridge melt inclusions correspond to entrapment pressures of ≤506 MPa (equivalent to 16.4 km below the seafloor) and ≤340 MPa (10.6 km) for plagioclase- and olivine- hosted melt inclusions respectively. In olivine, entrapment pressures correlate with host crystal morphology (Fig. 4), such that inclusions hosted within skeletal crystals (Fig. 1a) have lower CO_2 contents (<1000 ppm), and correspondingly lower pressures (<~145 MPa, or <3.6 km below the seafloor) than non-skeletal olivines, which preserve a range in entrapment pressures of 49-340 MPa (0.2-10.6 km below the seafloor).

For direct comparison, we examine data from three locations along the Gakkel Ridge where both olivine- and plagioclase-hosted melt inclusions have been analysed (31°E Basement Ridge, 18°50’ E Basement Ridge and 3°E Seamounts, Extended Data Figure 1; Fig. 5a-c). The data show a systematic offset in pressures, such that mean pressures are 215, 242 and 54 MPa higher in plagioclase-hosted melt inclusions than those recorded by olivine-hosted melt inclusions at the same location. This translates into mean depths of crystallisation that are 7, 9 and 2 km higher in plagioclase-hosted melt inclusions compared to olivine-hosted

melt inclusions, with only limited overlap between the two records. Critically, the difference between the melt inclusion pressures in the two phases is present in the dataset as a whole (Fig. 2 and Fig. 5e), in particular locations (Fig. 5a-c), and within individual samples (Fig. 5d and Extended Data Figure 4). This suggests that the difference is not controlled by local conditions, but instead reflects a fundamental difference in the pressure record of olivine- and plagioclase-hosted melt inclusions, with olivine being biased towards low pressures. There are three potential explanations for this difference. First, the entrapment pressures may be geologically significant and record crystallisation conditions within the magmatic system. Alternatively, the olivine data may be compromised by either decrepitation[15,25] or volatile loss into bubbles[26,27].

First, we examine the possibility of secondary volatile loss. If olivine and plagioclase are, respectively, tight and leaky vessels, one might expect olivine-hosted inclusions to record higher CO_2 contents, and in turn greater entrapment pressures, than plagioclase. However, Figures 2 and 5 demonstrate the opposite. Loss of CO_2 by decrepitation, or breaking of inclusions, is the more common explanation, and has been used to explain why 95% of olivine-hosted melt inclusions from a range of low-H_2O basaltic settings record similar, low entrapment pressures (≤200 MPa)[15]. Whilst this might explain the shallow pressures recorded by olivine-hosted melt inclusions, we see no physical evidence of decrepitation (e.g., melt filled fractures[28] and melt inclusion halos around larger melt inclusions[29]). Alternatively, CO_2 may be sequestered into bubbles[26,27] formed as result of post-entrapment crystallisation[30] or thermal contraction of the melt inclusion[25]. Either case would make the pressure estimates minima, as demonstrated in Figure 5b, which shows that the only analysed bubble-bearing plagioclase-hosted melt inclusion yields significantly lower pressures (88 MPa) than the remainder of inclusions in that host plagioclase (339-391 MPa). Similarly, the only analysed bubble-bearing olivine-hosted melt inclusion records slightly lower pressure (~52 MPa) than an inclusion in the same host with no visible bubble (~57 MPa; Fig. 1b). These observations, along with the absence of observed bubbles in most

measured melt inclusions, suggests that bubble formation does not control the melt inclusion pressure record. We conclude, therefore, that the lack of physical evidence of either decrepitation or bubbles, in combination with the preservation of high crystallisation pressures in plagioclase-hosted melt inclusions despite the assumed “leaky” nature of plagioclase, is inconsistent with a secondary cause for the difference in pressure between olivine- and plagioclase-hosted melt inclusions.

Textural analysis of the host crystals suggest that the data are recording geologic processes. Complex zoning patterns and abundant evidence of resorption in plagioclase attests to protracted growth histories within an open magmatic system. Whilst similar textures in the olivine hosts may have been erased by fast major element diffusion[17], the observation remains that there is a correlation between textural complexity and crystallisation pressures. In fact, 58% of olivine crystals hosting melt inclusions with <1000 ppm CO_2 have skeletal morphologies and record shallower mean crystallisation pressures (72 MPa) compared to host crystals with non-skeletal morphologies (178 MPa). This suggests that skeletal olivines formed in the shallow portion of the plumbing system, consistent with their inferred origin via rapid, late-stage growth. Interestingly, the olivine crystal with the highest melt inclusion crystallisation pressure (340 MPa; 10.6 km) forms part of a poly-mineralic glomerocryst (i.e., a crystal aggregate comprising more than one crystal phase) that also contains complexly zoned plagioclase crystals (Extended Data Figure 5).

The volatile data can be reconciled in a model where olivine and plagioclase experience different crystallisation histories, with plagioclase capturing multi-stage processes in a deep-seated crystal mush, and olivine forming predominantly during late stage crystallisation in shallower portions of the plumbing system. Whilst phase relationships show that olivine is the first phase to crystallise from mid-ocean ridge basalts, and therefore should record crystallisation at elevated pressures, the high density of olivine (3.2 gcm^{-3}) compared to that of plagioclase (~2.7 gcm^{-3}) and basaltic melt (~2.6 gcm^{-3}) may prevent its eruption from

deeper within the plumbing system. This would account for the sparsity of olivine-hosted melt inclusions that record pressures as high as those recorded by plagioclase-hosted melt inclusions. The poly-mineralic glomerocryst of high-pressure olivine intergrown with complexly zoned, resorbed plagioclase (Extended Data Figure 5) provides a direct snapshot of this olivine-plagioclase mush. Moreover, plagioclase crystallisation at depths as shallow as olivine is absent in the melt inclusion dataset at two of the three locations (Fig. 5a,b). We suggest that this may reflect an absence of analysable melt inclusions in plagioclase that crystallised shallowly. Indeed, whilst skeletal plagioclase in samples from both locations may represent shallow level crystallisation analogous to that recorded by skeletal olivine, these crystals do not contain analysable melt inclusions, as inclusions are either absent, too small or microcrystalline. Thus, textural observations of olivine and plagioclase host crystals suggest that the disparity between recorded crystallisation pressures is primary.

Our data provide important insights into the physical nature of magmatic systems at mid-ocean ridges and reveal, contrary to current constraints, that magmatic roots are vertically extensive, at least at ultraslow-spreading ridges. More specifically, the Gakkel Ridge magmatic system extends from the seafloor to at least 16.4 km. Moreover, the depth distribution revealed by plagioclase-hosted inclusions (Fig. 5) places most crystallisation in the lithospheric mantle. Finally, we have demonstrated that plagioclase-hosted melt inclusions preserve reliable vapour saturation pressures, and that plagioclase provides a comprehensive record of the deeper levels of crystallisation in magmatic systems. In contrast, olivine captures predominantly shallower levels. Hence, combined studies of olivine- and plagioclase-hosted melt inclusions will enable significantly improved reconstructions of the true extent of magma plumbing systems.

1. Crisp, J. A. Rates of magma emplacement and volcanic output. *J. Volcanol. Geotherm. Res.* **20,** 177–211 (1984).
2. Shaw, A. M., Behn, M. D., Humphris, S. E., Sohn, R. a. & Gregg, P. M. Deep pooling

of low degree melts and volatile fluxes at the 85°E segment of the Gakkel Ridge: evidence from olivine-hosted melt inclusions and glasses. *Earth Planet. Sci. Lett.* **289,** 311–322 (2010).

3. Wanless, V. D., Behn, M. D., Shaw, A. M. & Plank, T. Variations in melting dynamics and mantle compositions along the Eastern Volcanic Zone of the Gakkel Ridge: insights from olivine-hosted melt inclusions. *Contrib. to Mineral. Petrol.* **167,** 1005 (2014).
4. Colman, A., Sinton, J. M. & Wanless, V. D. Constraints from melt inclusions on depths of magma residence at intermediate magma supply along the Galápagos Spreading Center. *Earth Planet. Sci. Lett.* **412,** 122–131 (2015).
5. Wanless, V. D. & Shaw, A. M. Lower crustal crystallization and melt evolution at mid-ocean ridges. *Nat. Geosci.* **5,** 651–655 (2012).
6. Wanless, V. D. *et al.* Magmatic plumbing at Lucky Strike volcano based on olivine-hosted melt inclusion compositions. *Geochemistry, Geophys. Geosystems* 4692–4711 (2014). doi:10.1002/2015GC005918.
7. Wanless, V. D. & Behn, M. D. Spreading rate-dependent variations in crystallization along the global mid-ocean ridge system. *Geochemistry, Geophys. Geosystems* **116,** 1–12 (2017).
8. Schlindwein, V. & Schmid, F. Mid-ocean-ridge seismicity reveals extreme types of ocean lithosphere. *Nature* **535,** 276–279 (2016).
9. Chen, Y. J. & Lin, J. High sensitivity of ocean ridge thermal structure to changes in magma supply: The Galápagos Spreading Center. *Earth Planet. Sci. Lett.* **221,** 263–273 (2004).
10. Phipps-Morgan, J. & Chen, Y. J. The Genesis of Oceanic Crust: Magma Injection, Hydrothermal Circulation, and Crustal Flow. *J. Geophys. Res.* **98,** 6283–6297 (1993).
11. Lissenberg, C. J. & MacLeod, C. J. A reactive porous flow control on mid-ocean ridge magmatic evolution. *J. Petrol.* **57,** 2195–2220 (2016).
12. Kent, A. J. R. Melt Inclusions in Basaltic and Related Volcanic Rocks. *Rev. Mineral.*

Geochemistry **69,** 273–331 (2008).

13. Kress, V. C. & Ghiorso, M. S. Thermodynamic modeling of post-entrapment crystallization in igneous phases. *J. Volcanol. Geotherm. Res.* **137,** 247–260 (2004).
14. Neave, D. A., Hartley, M. E., Maclennan, J., Edmonds, M. & Thordarson, T. Volatile and light lithophile elements in high-anorthite plagioclase-hosted melt inclusions from Iceland. *Geochim. Cosmochim. Acta* **205,** 100–118 (2017).
15. MacLennan, J. Bubble formation and decrepitation control the CO_2 content of olivine-hosted melt inclusions. *J. Geophys. Res. Solid Earth* (2017). doi:10.2113/2.4.476
16. Grove, T. L., Baker, M. B. & Kinzler, R. J. Coupled CaAl-NaSi diffusion in plagioclase feldspar: experiments and applications to cooling rate speedometry. *Geochim. Cosmochim. Acta* **48,** 2113–2121 (1984).
17. Chakraborty, S. Rates and mechanisms of Fe-Mg interdiffusion in olivine at 980°–1300°C. *J. Geophys. Res.* **102,** 12317 (1997).
18. Bryan, W. B. Systematics of modal phenocryst assemblages in submarine basalts: petrologic implications. *Contrib. to Mineral. Petrol.* **83,** 62–74 (1983).
19. Welsch, B., Hammer, J. & Hellebrand, E. Phosphorus zoning reveals dendritic architecture of olivine. *Geology* **42,** 867–870 (2014).
20. Helo, C., Longpré, M.-A., Shimizu, N., Clague, D. A. & Stix, J. Explosive eruptions at mid-ocean ridges driven by CO_2-rich magmas. *Nat. Geosci.* **4,** 260–263 (2011).
21. Michael, P. J. & Graham, D. W. The behavior and concentration of CO_2 in the suboceanic mantle: Inferences from undegassed ocean ridge and ocean island basalts. *Lithos* **236–237,** 338–351 (2015).
22. Hartley, M. E., Maclennan, J., Edmonds, M. & Thordarson, T. Reconstructing the deep CO_2 degassing behaviour of large basaltic fissure eruptions. *Earth Planet. Sci. Lett.* **393,** 120–131 (2014).
23. Le Voyer, M., Kelley, K. A., Cottrell, E. & Hauri, E. H. Heterogeneity in mantle carbon content from CO_2 -undersaturated basalts. *Nat. Commun.* **8,** (2017).

24. Matthews, S., Shorttle, O., Rudge, J. F. & Maclennan, J. Constraining mantle carbon: CO2-trace element systematics in basalts and the roles of magma mixing and degassing. *Earth Planet. Sci. Lett.* **480,** 1–14 (2017).

25. Lowenstern, J. B. Applications of silicate-melt inclusions to the study of magmatic volatiles. *Magmas, Fluids Ore Depos. Mineral. Assoc. Canada Short Course* **23,** 71–99 (1995).

26. Anderson, A. T. & brown, Georgia, G. CO_2 contents and formation pressures of some Kilauean melt inclusions. *Glass* **78,** 794–803 (1993).

27. Wallace, P. J., Kamenetsky, V. S. & Cervantes, P. Melt inclusion CO_2 contents, pressures of olivine crystallization, and the problem of shrinkage bubbles. *Am. Mineral.* **100,** 787–794 (2015).

28. Roedder, E. Liquid CO_2 inclusions in olivine-bearing nodules and phenocrysts from basalts. *Am. Mineral.* **50,** 356–366 (1965).

29. Portnyagin, M. V, Plechov, P. Y., Matveev, S. V, Osipenko, A. B. & Mironov, N. L. Petrology of avachites, high-magnesian basalts of Avachinsky volcano, Kamchatka: I. General characteristics and composition of rocks and minerals. *Petrologiya* **13,** 99–121 (2005).

30. Roedder, E. Fluid Inclusions. *Rev. Mineral.* (1984).

Supplementary Information is linked to the online version of the paper at www.nature.com/nature.

Acknowledgements

We thank H.J.B. Dick for providing access to Gakkel Ridge samples, C-J. de Hoog for expert advice on SIMS analysis, D. Muir for assistance with the EDS analysis, and A. Oldroyd for

help with sample preparation. We also thank Mark Behn and an anonymous reviewer for their comments on the original manuscript. This research was supported by NERC grants NE/L002434/1 (E.N.B.), NE/R001332/1 (M-A.M) and NE/M000427/1 (F.E.J) and IMF641/1017 (C.J.L.) and by an AXA Professorship and Wolfson Merit Award to K.V.C.

Author contributions

E.N.B. and C.J.L. conceived of the study. E.N.B. collected all data, except melt inclusion trace element data collected by F.E.J. E.N.B. wrote the manuscript under supervision of C.J.L. K.V.C., M-A.A. and F.E.J contributed to critical discussions and commented on the manuscript.

Author Information

Reprints and permissions

Reprints and permissions information is available at www.nature.com/reprints.

Competing interests

The authors declare no competing interests.

Corresponding author

Correspondence and requests for materials should be addressed to bennette7@cardiff.ac.uk or LissenbergCJ@cardiff.ac.uk.

Figure 1 **Textural complexity of olivine and plagioclase and melt inclusion distribution and associations.** Backscattered electron images of olivine (**a**-**c**) and plagioclase (**d**-**i**). Scale bars are 100 μm (**b**,**c**,**f**,**g**) and 250 μm (**a**,**d**,**e**,**h**,**i**). White arrows indicate resorption (**f**). Numbers correspond to analysed melt inclusions highlighted in Supplementary Table 2.

Figure 2 **Volatile contents of Gakkel Ridge olivine- and plagioclase-hosted melt inclusions.** CO_2 versus H_2O for Gakkel Ridge plagioclase- (circles) and olivine- (diamonds)

hosted melt inclusions. Black outlined points are from this study; those from 85°Seamount are from ref. 2, points with no outlines are from ref. 3. Grey fields include the following data: Lucky Strike volcano on the Mid-Atlantic Ridge (MAR)[6]; Galapagos Spreading Centre (GSC)[4]; Juan de Fuca Ridge (JDF) and East Pacific Rise (EPR)[5]. Comparative datasets have all used volatiles to investigate crystallisation pressures and are from on-axis locations.

Figure 3 **Relationship between melt inclusion Mg# and CO_2 content (a,b) and Ba vs. CO_2/Ba of plagioclase- and olivine-hosted melt inclusions (c,d).** Comparative data sources are as follows: (**a**) plagioclase-hosted MI data from Helo et al.[20] (grey points); (**c,d**) Global MORB glasses[2,3,21]; Gakkel Ridge MIs[2,3]; Juan de Fuca (JdF) Ridge MIs[20]; Laki, Iceland MIs[22]; Mid-Atlantic Ridge MIs[23]. Note: Inclusion locations in **b** are unclassified if MIs come from either a broken host crystal, or from a host crystal where no back-scattered electron image exists to allow the locations to be assigned based on compositional zoning.

Figure 4 **Crystallisation depth and pressures recorded in olivine.** Histogram showing the difference in the distribution of crystallisation depths recorded in skeletal (dots) and non-skeletal (grey) olivine. The one bubble-bearing melt inclusion analysed plots at 0 km. Pressures correspond to the pressure below the seafloor.

Figure 5 **Comparison of crystallisation depths recorded in melt inclusions.** Histograms showing the distribution of crystallisation depths recorded in olivine- and plagioclase-hosted melt inclusions at three locations along the Gakkel Ridge (31°E Basement Ridge, **a**; 18°50' Basement Ridge, **b**; and 3°E Seamounts, **c**). **d** Comparison of pressures recorded by olivine- and plagioclase-hosted melt inclusions in a single sample (HLY0102-D48-SG) from 31°E Basement Ridge; olivine data here are from ref. 3. All data are compared in **d**. Pressures correspond to the pressure below the seafloor. Olivine, Ol; plagioclase, Pl.

Methods

Melt inclusions volatile analysis. Melt inclusion CO_2, H_2O, K_2O and B contents were measured using the Cameca IMS4f ion microprobe at the Edinburgh Ion Microprobe Facilty. A ~5 nA $^{16}O^-$ primary beam with a 14.5 kV impact energy beam was used. Melt inclusions were analysed for CO_2 first in a separate measurement before H_2O and other elements, with CO_2 measured at high mass resolution ($M/\Delta M = 1200$) sufficient to avoid interference between $^{24}Mg^{2+}$ and $^{12}C^+$. Energy filtering of the secondary ions was applied, using offsets of 75 eV and 50 eV for H_2O and CO_2, respectively, using a 50 eV energy window. Image fields of 25 μm and 50 μm and field apertures with effective diameters of 8 μm and 16 μm were used during H_2O and CO_2 analysis, respectively. Prior to each measurement the beam was aligned relative to the centre of the field aperture. H_2O and CO_2 target locations were rastered for 2 and 4 minutes prior to each analysis using analysis beam conditions to remove surface contamination; during this time peak mass positions were centred. Each analysis ran for 4 minutes following rastering. For H_2O and CO_2 measurements, counts were normalised to ^{30}Si and corrected for known SiO_2 content of the samples, except $^1H/^{30}Si$ as this has been shown to have a matrix effect proportional to the material's SiO_2 content. The analyses were calibrated against a set of basaltic glass standards of known CO_2 (0-2183 ppm) and H_2O (0.00-3.07 wt.%) contents[31]. Instrumental blank measurements for H_2O and CO_2 were made on plagioclase in each mount and subtracted from the raw count rates: targets in 12 mounts were analysed. Uncertainty and accuracy of SIMS analysis can be found in Supplementary Table 1 and Extended Data Figure 6 respectively. Raw volatile element data are present in Supplementary Table 2.

Melt inclusion and host crystal major element analysis. Following ion microprobe analysis, melt inclusions and their host crystals were analysed using Cardiff's Zeiss Sigma HD field emission gun SEM, which is equipped with two 150mm^2 Oxford Instruments X-MaxN silicon drift EDS detectors. A 1 nA beam current, 20.0 kV accelerating voltage, fixed working distance of 8.9 mm and 60 nm aperture were used. EDS spectra were acquired

over 20s live time using both detectors with an output count rate of ~136 kcps. A defocused beam rastering over 5-10 μm^2 areas was used to minimise Na loss in both plagioclase and melt inclusions. Oxford Instruments Aztec Software was used to process and quantify raw data using the internal XPP matrix correction. A total of 30 olivine-hosted and 75 plagioclase-hosted melt inclusions and their hosts were analysed. Host An and Fo content and glass major element compositions are reported in Supplementary Table 2. All analysed melt inclusions were ≥20μm in diameter and glassy. A comprehensive suite of standards were used to calibrate EDS analysis of all mineral phases and glass. Supplementary Tables 3 and 4 report the precision and accuracy of glass and mineral secondary standard measurements. Back-scattered electron images of each inclusion and host crystal were acquired to assess whether inclusions showed signs of crystallisation and if hosts showed evidence of compositional zoning.

Melt inclusion trace element analysis. Following major element analysis, melt inclusions were analysed using LA-ICP-MS (Photon Machines G2 193 nm excimer laser system coupled to an Agilent 8800 ICP-MS/MS) at the School of Environment, Earth and Ecosystem Sciences (The Open University). NIST SRM 612 was used for external calibration of data (values given in Jenner and O'Neill (ref.32) and ^{43}CaO for internal calibration. Operating conditions (20 seconds of background and 20 seconds of ablation) for analysis of ^{51}V, ^{85}Rb, ^{89}Y, ^{90}Zr, ^{93}Nb, ^{137}Ba, ^{139}La, ^{140}Ce, ^{146}Nd, ^{147}Sm, ^{153}Eu, ^{157}Gd, ^{163}Dy, ^{165}Ho, ^{166}Er, ^{172}Yb and ^{175}Lu utilised a 10Hz repetition rate; an ablation diameter of 20 μm; a fluency of 3.63 J/cm2 on the sample surface; and ablation cell gas of 0.9 l min-1 He. BCR-2G was used as a secondary standard to monitor accuracy and precision of data. Repeat analyses of BCR-2G (Supplementary Table 5) analysed during the same analytical shift as the Gakkel melt inclusions show excellent precisions (average of <3% percentage relative standard deviation) and accuracy (typically within 3% of preferred values).

Melt inclusion corrections. The major and volatile element compositions of both olivine- and plagioclase-hosted melt inclusions were corrected for the effects of post-entrapment crystallisation (PEC). Raw and corrected melt inclusion compositions (major and volatile elements) are reported in Supplementary Table 2. Olivine compositions were corrected by iteratively adding equilibrium olivine back into the melt until the melt and host olivine were in equilibrium with one another[33]. This assumed an equilibrium Fe-Mg distribution coefficient (K_D) of 0.3 and $Fe^{3+}/\Sigma Fe$ of 0.1[34]. Olivine PEC corrections range from 2-22% (median 13.0%) (Supplementary Table 2). To date there is no widely accepted method of correcting PEC in plagioclase-hosted melt inclusions. Previously, PEC corrections have been undertaken by adding plagioclase (equilibrium plagioclase or host plagioclase) to the melt inclusion until its MgO-Al_2O_3[14] or TiO_2-Al_2O_3[35] systematics are consistent with regressions through Icelandic glass arrays. However, these corrections are unconstrained in that the melt inclusion compositions can move in both MgO or TiO_2 and Al_2O_3 space toward these regressions. Here we employed an empirical correction which assumes that during plagioclase crystallisation, Al_2O_3 is the most modified melt component, whilst Mg# remains unchanged because both Mg and Fe are incompatible in plagioclase. Plagioclase was therefore added to the melt inclusion composition until the melt inclusions met the Al_2O_3 content (at a given Mg#) of the combined Gakkel glass[36,37] (see Extended Data Figure 7 caption) and olivine-hosted melt inclusions[2,3] datasets. In practice we created a pseudo-liquid line of decent (see Extended Data Figure 7 caption for details) and then iteratively added host plagioclase compositions to the melt inclusions until this liquid line of decent was intersected. Plagioclase-hosted melt inclusion PEC corrections ranged from 0-41.5% (median 14.8%) (Supplementary Table 2). This approach has two benefits over previous approaches: (1) Mg# does not change during the correction and therefore the melt inclusion composition only changes vertically in Al_2O_3 space; and (2) the addition of the line drawn through the olivine-hosted melt inclusion data to create the pseudo-liquid line of decent prevents corrections that would result in melt inclusion compositions with unrealistically high Al_2O_3 contents

compared to the Gakkel glass and olivine-hosted melt inclusion arrays. To test the effect of the choice of pseudo-liquid line of decent, a second pseudo-liquid line of decent passing through the olivine-hosted melt inclusion data was used for a second correction; new PEC corrections range from 0-37.5% (median 11.5%). It can be seen from Extended Data Figure 7d that pressures calculated from this second PEC correction show negligible change from those calculated following the first PEC correction. There is no correlation between the percentage correction and calculated depth of crystallisation (Extended Data Figure 8).

Melt inclusion vapour saturation. To use melt inclusion volatile contents to determine crystallisation pressures, melt inclusions need to be vapour-saturated. If melts are undersaturated, pressures determined from their volatile contents will be underestimates[38]. Conversely, if melts are oversaturated, pressures will be overestimates. Although it has been argued that many mid-ocean ridge melt inclusions are CO_2 saturated[5], it has been suggested that CO_2-rich plagioclase-hosted melt inclusions from the Juan de Fuca Ridge are CO_2-oversaturated[20]. Hence, it is important to determine if the melt inclusions studied in this paper are vapour saturated. Several lines of evidence indicate that the Gakkel melt inclusions, including those populations with the highest CO_2 contents, are CO_2 saturated. Firstly, melt inclusions from the locations where the highest CO_2 contents were measured show a positive correlation between Mg# and CO_2 (Fig. 3a). This indicates that these inclusions preserve evidence for the occurrence of simultaneous degassing and crystallisation, suggesting that melts were saturated at the time of entrapment. The CO_2-oversaturated plagioclase-hosted melt inclusions from the Juan de Fuca ridge show no such correlation. Secondly, CO_2/Ba systematics of the Gakkel Ridge melt inclusions can be assessed and compared to a global compilation of glass and melt inclusions data (Fig. 3c,d). The maximum CO_2/Ba content of Gakkel Ridge melt inclusion (145) is in good agreement with current estimates of the CO_2/Ba content of the depleted mantle (~140: ref. 24). If our melt inclusions were oversaturated in CO_2, melt inclusions would have CO_2/Ba ratios above mantle values due to excess CO_2 at a given Ba content. This is indeed observed for the

CO_2-oversaturated Juan de Fuca melt inclusions[20] (grey arrow in Fig. 3c). In contrast, all Gakkel Ridge melt inclusions have CO_2/Ba ratios <145 and fall within the global MORB array (comprised of lavas as well as melt inclusions) for CO_2/Ba, indicating that they are not oversaturated and instead reflect varying degrees of degassing from mantle CO_2 values.

Saturation pressure calculation and depth conversion. Following correction for post-entrapment crystallisation (PEC) of major and volatile elements, vapour saturation pressures were calculated using MagmaSat[39]. Melt inclusions with visible bubbles were avoided, however, because polished blocks were used during ion microprobe analysis, the presence or absence of vapour bubbles deeper inside the inclusions could not be determined. Because these vapour bubbles may sequester CO_2[26,27], pressures determined from melt inclusions here are minima. Pressures were converted to crystallisation depths accounting for the pressure of the overlying water and crust, assuming a crustal density of 2.9 g/cm^3.

Saturation (i.e., entrapment) pressures recorded by olivine-hosted melt inclusions from mid-ocean ridge have to date been determined almost exclusively using VolatileCalc[40]. This is a mixed H_2O-CO_2 solubility model based on parameterisations of Dixon[38]. This model uses melt temperature and, SiO_2, CO_2 and H_2O content of the melt to calculate the saturation pressure. However, this model only allows SiO_2 contents between 40-49 wt.% SiO_2 and thus does not account for compositional variability present at a given SiO_2 content. MagmaSat[39], a thermodynamic mixed CO_2-H_2O model, is calibrated for H_2O and CO_2 solubility and mixed fluid saturation in silicate melts. A benefit of this model is that it accounts for the effects of melt composition on H_2O-CO_2 solubility. When pressures are calculated with VolatileCalc using the SiO_2 specific to that inclusion, pressures are lower than with the default 49 wt.% because CO_2 solubility increases with reduced SiO_2[41] (Extended Data Figure 9).

Mantle CO_2 contents. The CO_2 content of the mantle has received considerable attention in recent years[3,21,23,24]. Whilst early studies used CO_2/Nb ratios to estimate the CO_2 content of

the mantle[42], recent studies have suggested that C behaves more like Ba than Nb[21,43]. Using CO_2-trace element systematics, Matthews et al. (ref.24) have shown that available data are consistent with the depleted mantle having a CO_2/Ba ratio of ~140; the maximum CO_2/Ba ratio of melt inclusions in our data, 145, is consistent with this estimate (Fig. 3c,d). Assuming a Ba content of 0.563 ppm for the depleted MORB mantle[44], the maximum CO_2/Ba ratio of 145 corresponds to a mantle CO_2 content of ~82ppm; this is within error of CO_2 content of the depleted MORB mantle calculated by Rosenthal et al. (ref.43).

31. Shishkina, T. A., Botcharnikov, R. E., Holtz, F., Almeev, R. R. & Portnyagin, M. V. Solubility of H_2O- and CO_2-bearing fluids in tholeiitic basalts at pressures up to 500MPa. *Chem. Geol.* **277,** 115–125 (2010).
32. Jenner, F. E. & O'Neill, H. S. C. Major and trace analysis of basaltic glasses by laser-ablation ICP-MS. *Geochemistry, Geophys. Geosystems* **13,** 1–17 (2012).
33. Sobolev, A. V. & Shimizu, N. Ultra-depleted primary melt included in an olivine from the Mid-Atlantic Ridge. *Lett. to Nat.* **363,** 151–154 (1993).
34. Berry, A. J., Stewart, G. A., O'Neill, H. S. C., Mallmann, G. & Mosselmans, J. F. W. A re-assessment of the oxidation state of iron in MORB glasses. *Earth Planet. Sci. Lett.* **483,** 114–123 (2018).
35. Hartley, M. E., Bali, E., MacLennan, J., Neave, D. A. & Halldorsson, S. A. Melt inclusion constraints on volatile systematics and degassing history of the 2014–2015 Holuhraun eruption, Iceland. *Contrib. to Mineral. Petrol.* **173,** 1–23 (2018).
36. Lehnert, K., Su, Y., Langmuir, C. H., Sarbas, B. & Nohl, U. A global geochemical database structure for rocks. *Geochemistry Geophys. Geosystems* **1,** 1 (2000).
37. Lissenberg, C. J., MacLeod, C. J. & Bennett, E. N. Consequences of a crystal mush-dominated magma plumbing system: a mid-ocean ridge perspective. *Philos. Trans. R. Soc. A Math. Phys. Eng. Sci.* (2018). doi:10.1098/rsta.2018.0014
38. Dixon, J. E. & Stolper, E. M. An experimental study of water and carbon dioxide

solubilities in mid-ocean ridge basaltic liquids.Part II: Applications to degassing. *J. Petrol.* **36,** 1633–1646 (1995).

39. Ghiorso, M. S. & Gualda, G. A. R. An H_2O–CO_2 mixed fluid saturation model compatible with rhyolite-MELTS. *Contrib. to Mineral. Petrol.* **169,** 1–30 (2015).
40. Newman, S. & Lowenstern, J. B. Volatile Calc : a silicate melt – H_2O – CO_2 solution model written in Visual Basic for excel. *Comput. Geosci.* **28,** 597–604 (2002).
41. Shishkina, T. A. *et al.* Compositional and pressure effects on the solubility of H_2O and CO_2 in mafic melts. *Chem. Geol.* **388,** 112–129 (2014).
42. Saal, A. E., Hauri, E. H., Langmuir, C. H. & Perfit, M. R. Vapour undersaturation in primitive mid-ocean-ridge basalt and the volatile content of Earth's upper mantle. *Nature* **419,** 451–455 (2002).
43. Rosenthal, A., Hauri, E. H. & Hirschmann, M. M. Experimental determination of C, F, and H partitioning between mantle minerals and carbonated basalt, CO_2/Ba and CO_2/Nb systematics of partial melting, and the CO_2 contents of basaltic source regions. *Earth Planet. Sci. Lett.* **412,** 77–87 (2015).
44. Workman, R. K. & Hart, S. R. Major and trace element composition of the depleted MORB mantle (DMM). *Earth Planet. Sci. Lett.* **231,** 53–72 (2005).
45. Jakobsson, M *et al.* The International Bathymetric Chart of the Arctic Ocean (IBCAO) Version 3.0. *Geophys. Res. Lett.* **39,** 1-6 (2012).
46. Ryan, W. B. F. *et al.* Global multi-resolution topography synthesis. *Geochemistry, Geophys. Geosystems* **10,** (2010).

Data availability

Source data for all figures are provided with the paper and also in supplementary information tables. The data is also available from EarthChem with the following DOI: 10.1594/IEDA/111315

Extended Data Figure 1**: Sample locations along the Gakkel Ridge.** Symbol colours are as follows: green, new plagioclase- and olivine-hosted melt inclusion analysis; orange, new plagioclase-hosted melt inclusion data supplemented by olivine-hosted melt inclusion data

from ref. 3; purple and yellow points indicate data from ref. 2 and 3 respectively. Location name abbreviations are as follows: AVR, Axial Volcanic Ridge; SM, Seamount; BR, Basement Ridge; DSF, Deep Seafloor. IBCAO bathymetric data from ref. 45. The Global Multi-Resolution Topography (GMRT) synthesis[46] base map underlies IBCAO bathymetry. Map made using GeoMapApp (http://www.geomapapp.org).

Extended Data Figure 2**: Textural complexity of olivine and plagioclase and melt inclusion distribution.** Backscattered electron images of plagioclase (**a**-**c**) and olivine (**d**-**f**). Plagioclase can be unzoned (**c**), or show patchy (**a**), reverse and normal zoning (**b**); plagioclase show both internal (**a**,**b**) and external (**c**) resorption. Olivine is present in poly- and mono-mineral glomerocrysts (**d,e**) and as individual skeletal crystals (**f**); reverse (**d**) and normal (**e**) zoning is present. Scale bars are all 100 μm. Dashed red and yellow lines in **b** and **d** show the locations of resorption. Numbers correspond to analysed melt inclusions highlighted in Supplementary Table 2.

Extended Data Figure 3**: Relationship between melt inclusion size and CO_2 content.** Both plagioclase- and olivine-hosted melt inclusions show no relationship between melt inclusion size and CO_2 content.

Extended Data Figure 4: **Crystallisation depths recorded by melt inclusions from individual samples.** Within each sample, plagioclase records greater crystallisation depths than olivine. The three individual samples are from the 31°E Basement Ridge (HLY0102-D95-11 and HLY0102-D48-SGB), and 3°E Seamounts (HLY0102-D27-8).

Extended Data Figure 5**: Textural relationship of high-pressure olivine-hosted melt inclusion. a** Phase map showing the association of the high-pressure olivine-hosted melt inclusion with plagioclase. White lines delineate grain boundaries. Plagioclase exhibits

complex zoning (e.g., oscillatory (OZ) and patchy zoning (PZ) (**b, c**)). Plagioclase exhibits both internal and external resorption (IR and ER respectively) (**b, c**). Large amoeboid melt inclusions (**c**) also suggest the occurrence of resorption. Plagioclase melt inclusions were microcrystalline and hence not analysed for their volatile contents. Scale bars are 500 μm. For information relating to phase map acquisition, the reader is directed to ref. 37.

Extended Data Figure 6**: Calibration curves for CO_2 and H_2O SIMS analysis.** Calibration curves for both H_2O (**a**) and CO_2 (**b**). The different coloured lines in each panel indicate different sessions.

Extended Data Figure 7**: Plagioclase-hosted melt inclusion post-entrapment crystallisation correction.** Plagioclase-hosted melt inclusion compositions were empirically corrected for post-entrapment crystallisation (PEC). Host plagioclase compositions were added to the melt inclusions iteratively until the melt inclusions met the Al_2O_3 content (at a given Mg#) of the pseudo-liquid line of decent. The pseudo-liquid line of decent comprises two parts. Firstly a regression through Gakkel glass data[36,37] (black line), and secondly a hand-picked line that runs along the top of olivine-hosted melt inclusions[2,3] and Gakkel glass data (red line) (**a**). A second PEC correction was undertaken using a different pseudo-liquid line of decent (green line) (**c**) that resulted in lower corrections. A comparison of pressures calculated following each of these PEC corrections shows there is negligible difference in pressures calculated from the resulting melt compositions (**d**). Gakkel glass data were downloaded from the PetDB[36] Database (www.earthchem.org/petdb) on 15 July 2016.

Extended Data Figure 8**: Relationship between PEC correction and crystallisation depths.** There is no relationship between the magnitude of PEC correction and crystallisation depth.

Extended Data Figure 9**: Comparison between VolatileCalc and MagmaSat H_2O-CO_2 models.** The majority of melt inclusions have SiO2 >49 wt.% hence VolatileCalc pressures were calculated using a default SiO_2 value (49 wt.%; orange points). Where SiO_2 <49 wt.%, specific VolatileCalc pressures were calculated (blue points); blue points correspond to orange points with no outline calculated with the default SiO_2 content. VolatileCalc pressures are lower when the specific SiO_2 (not default 49 wt.% SiO_2) content of the melt inclusion is used.

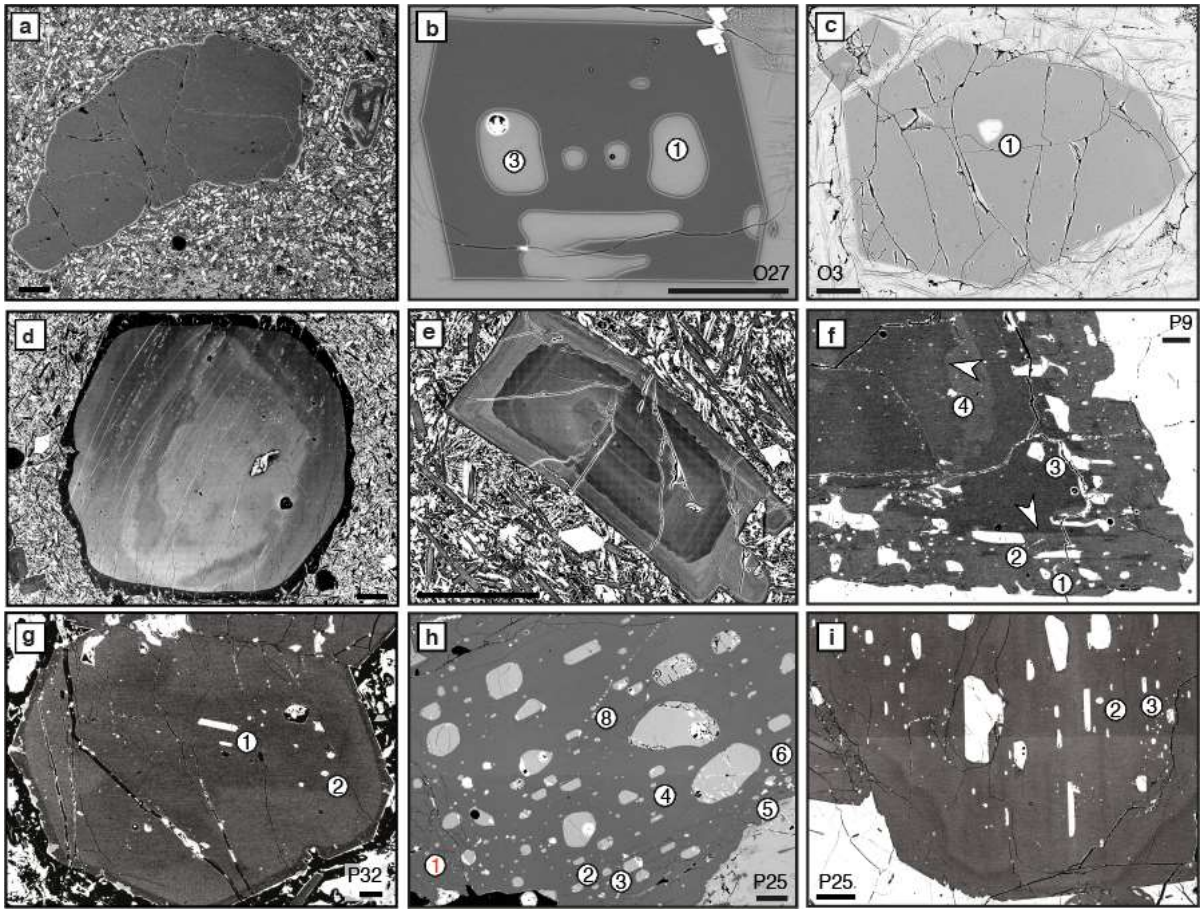

Main Text Figure 1.

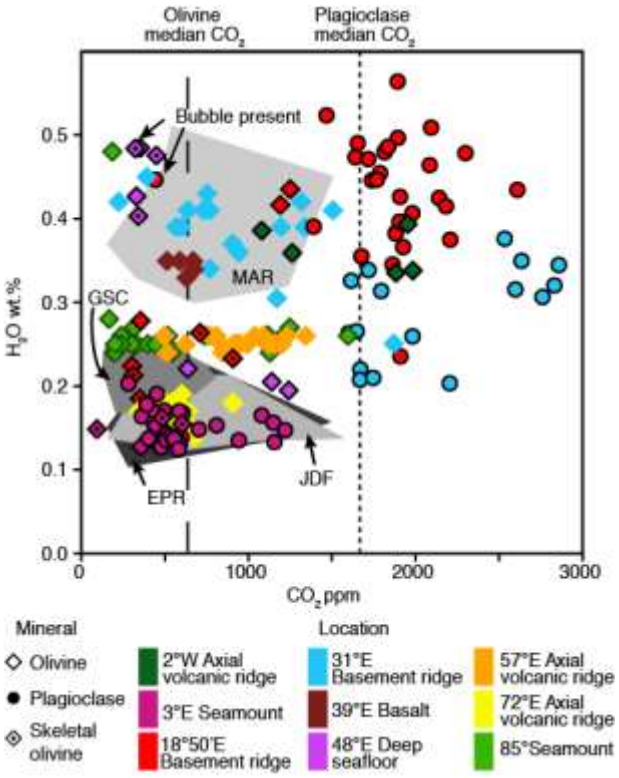

Main Text Figure 2.

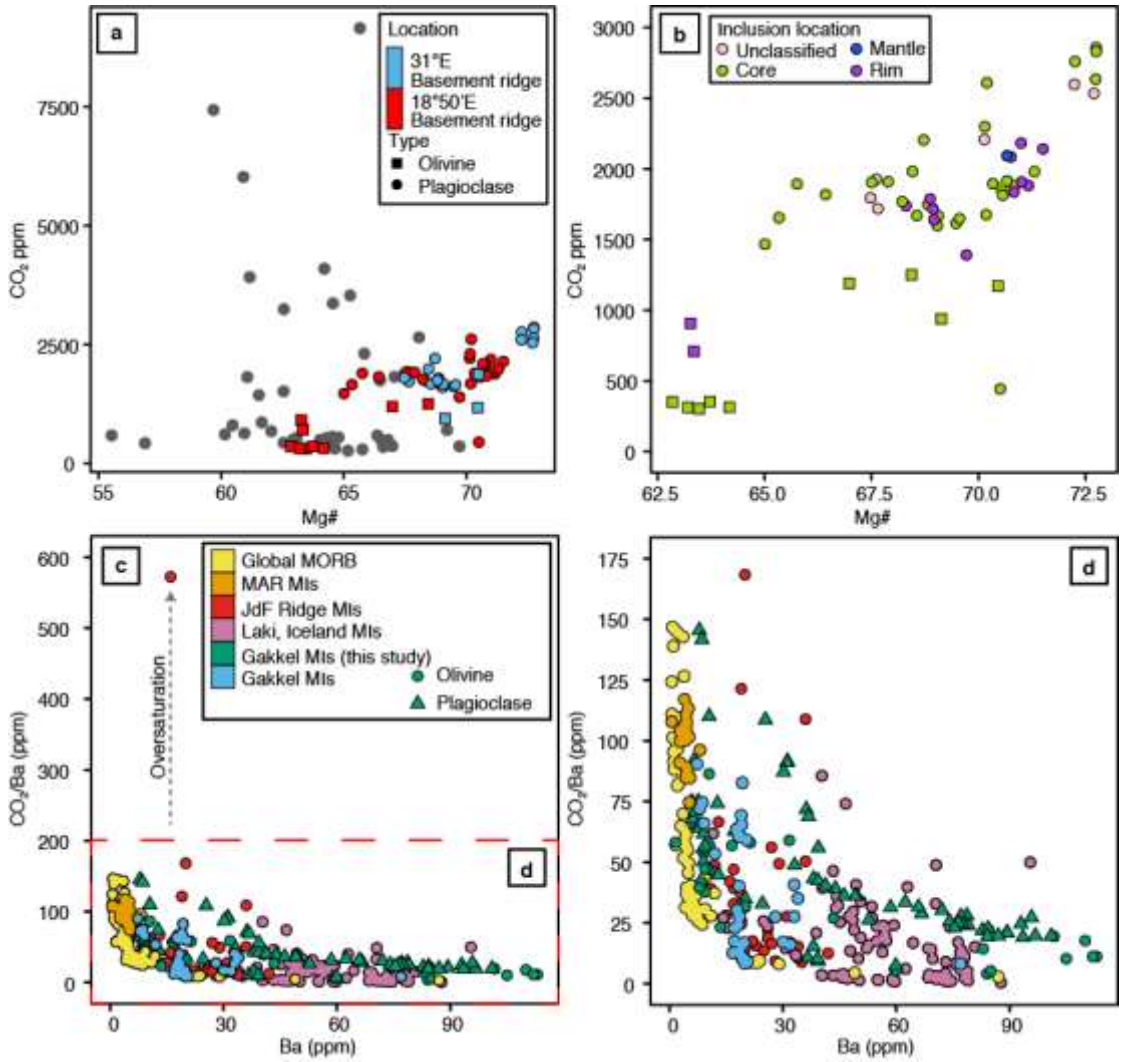

Main Text Figure 3.

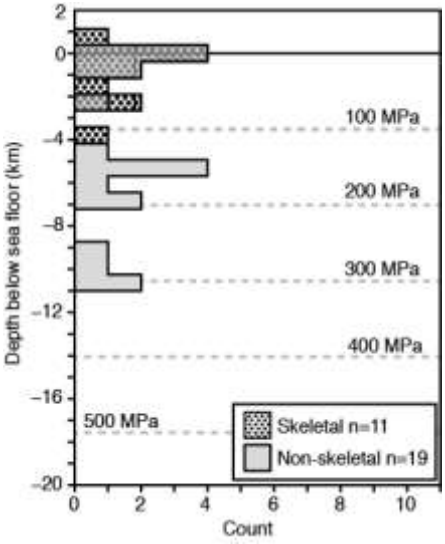

Main Text Figure 4.

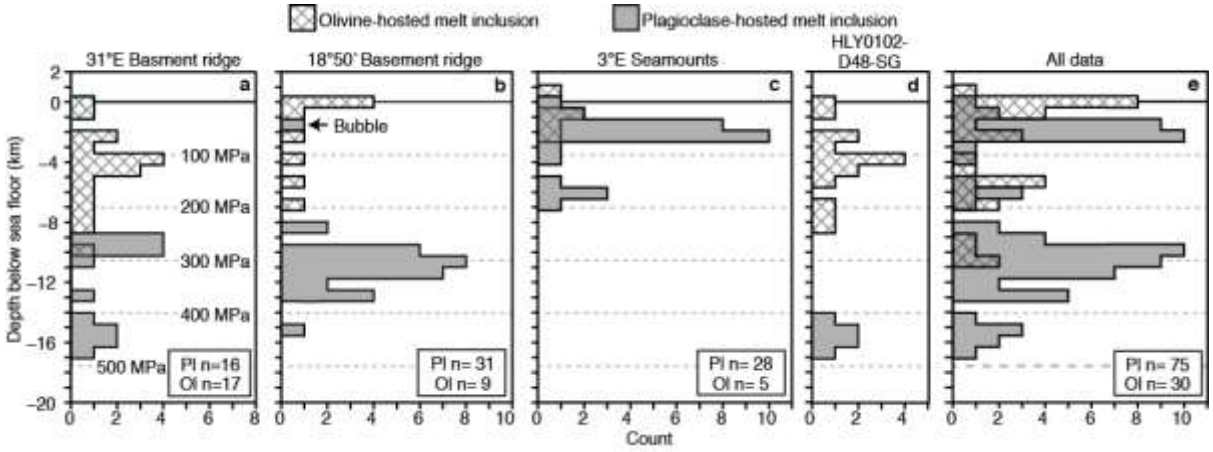

Main Text Figure 5.

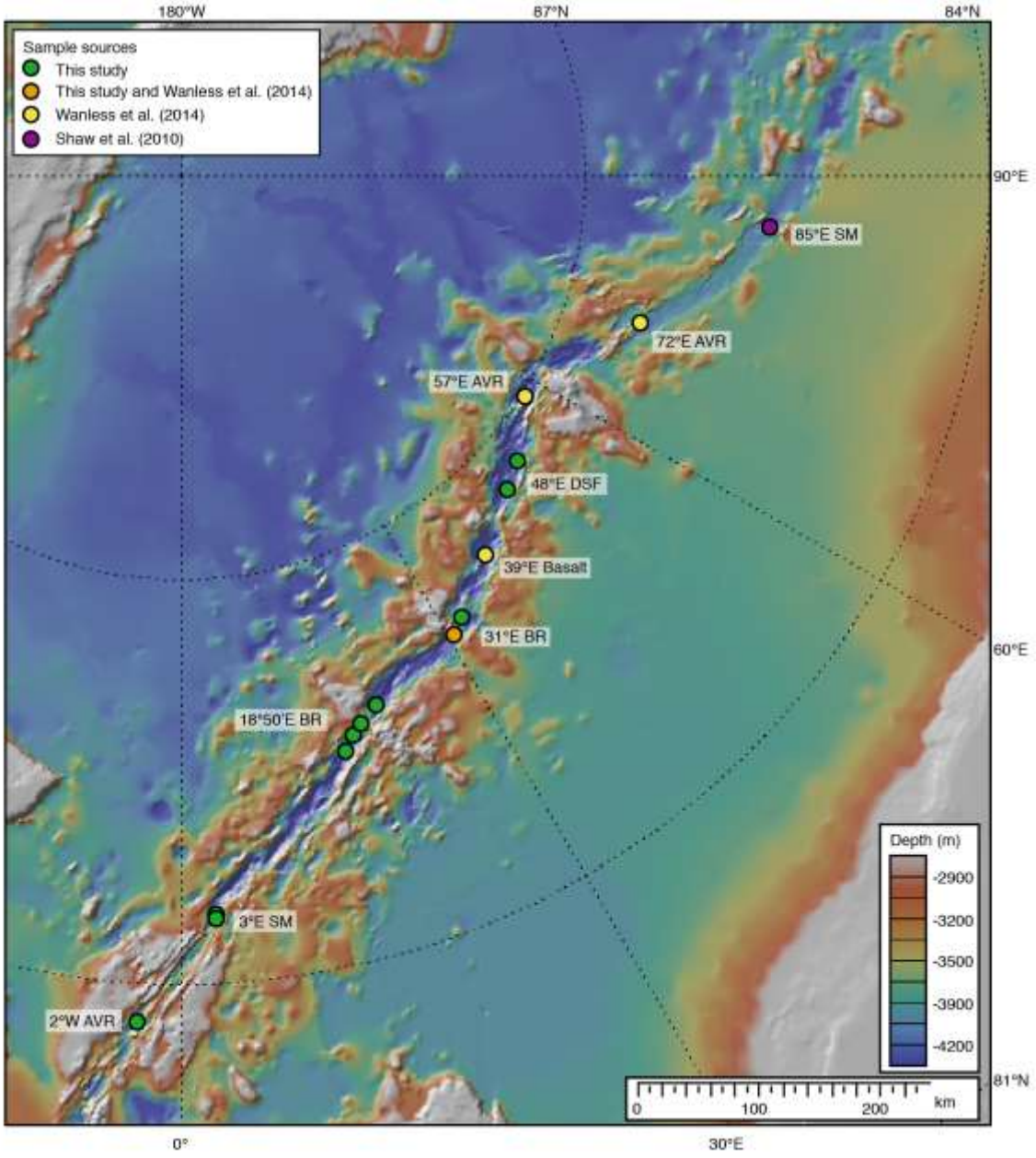

Extended Data Figure 1.

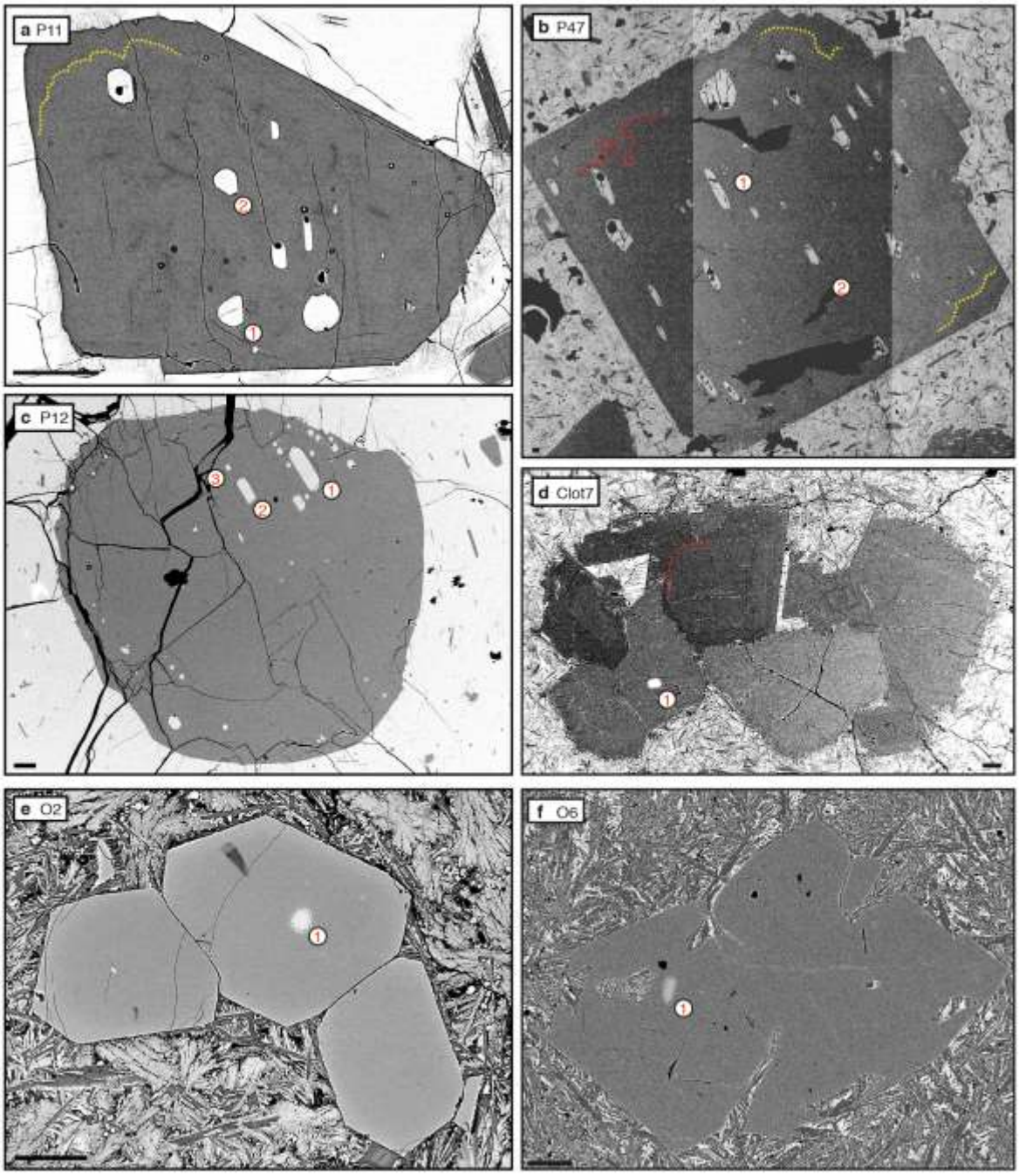

Extended Data Figure 2.

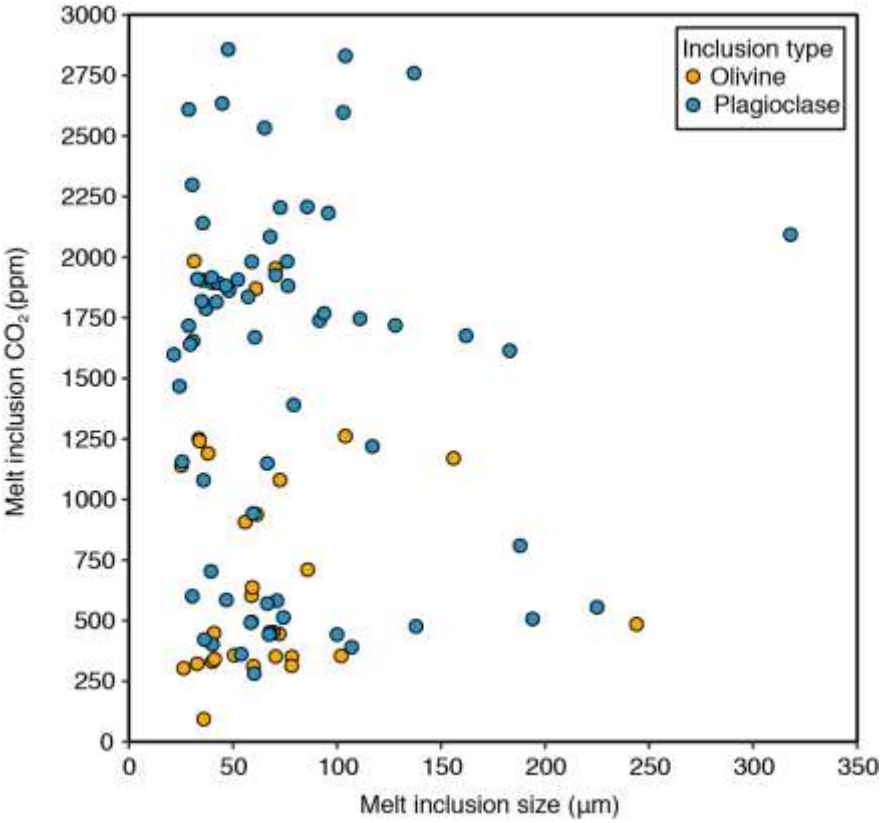

Extended Data Figure 3.

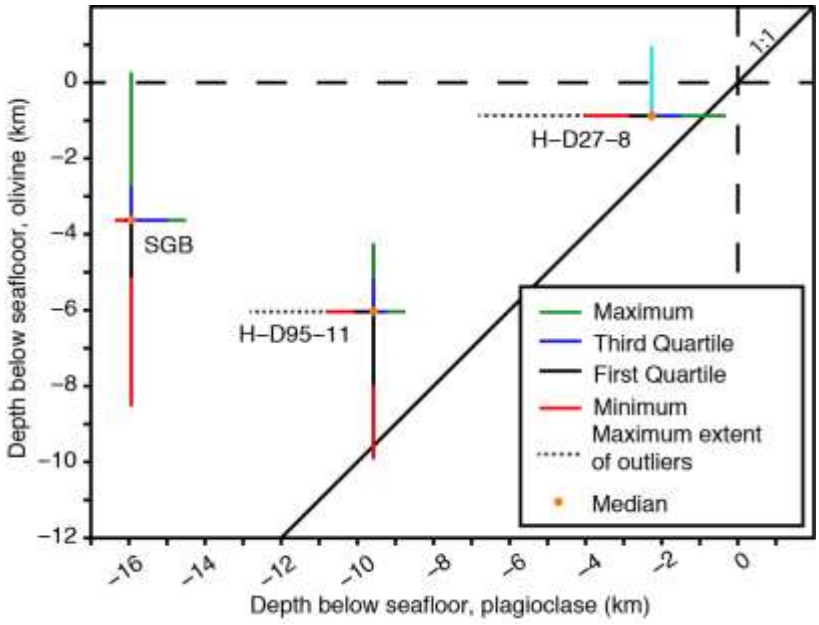

Extended Data Figure 4.

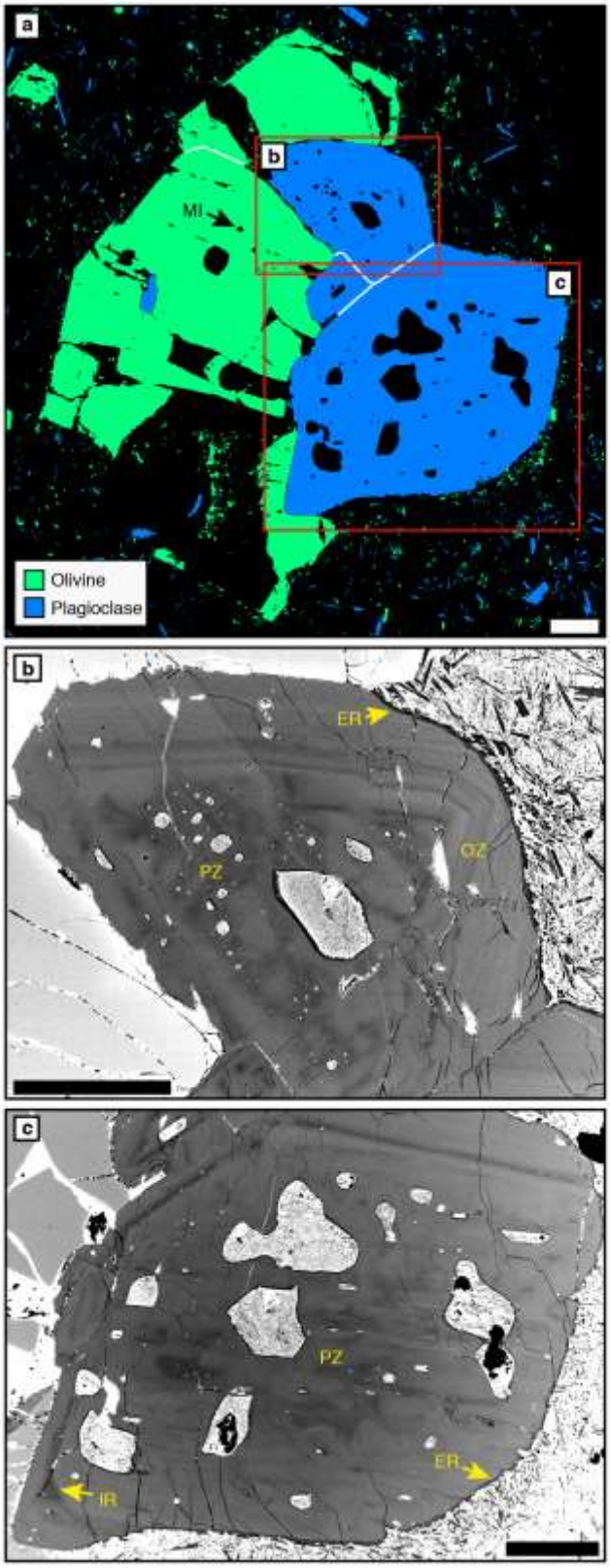

Extended Data Figure 5.

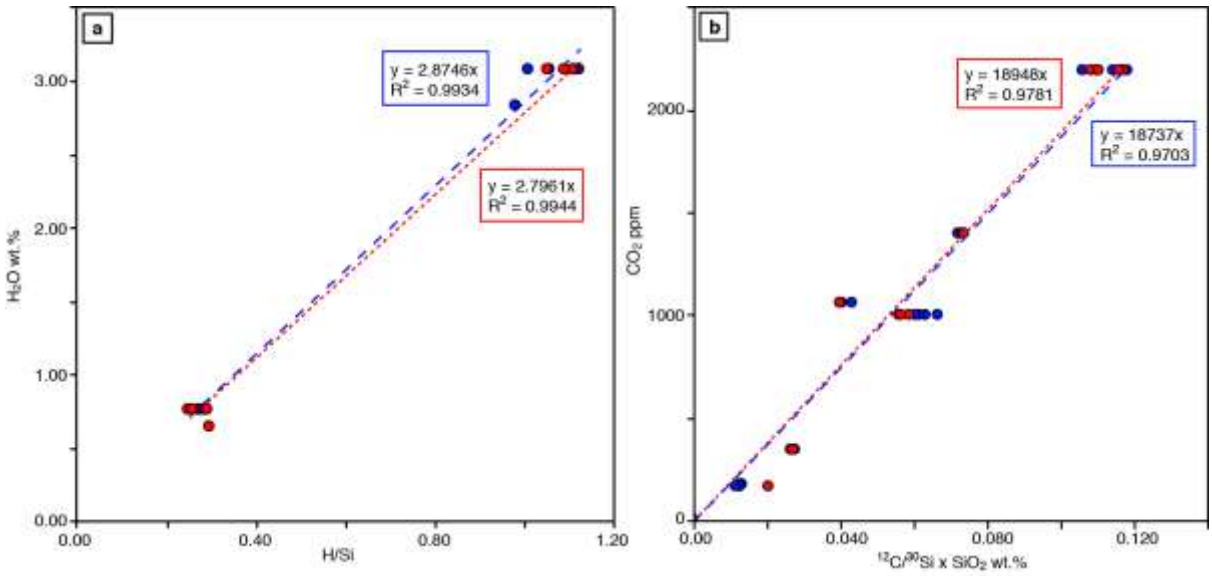

Extended Data Figure 6.

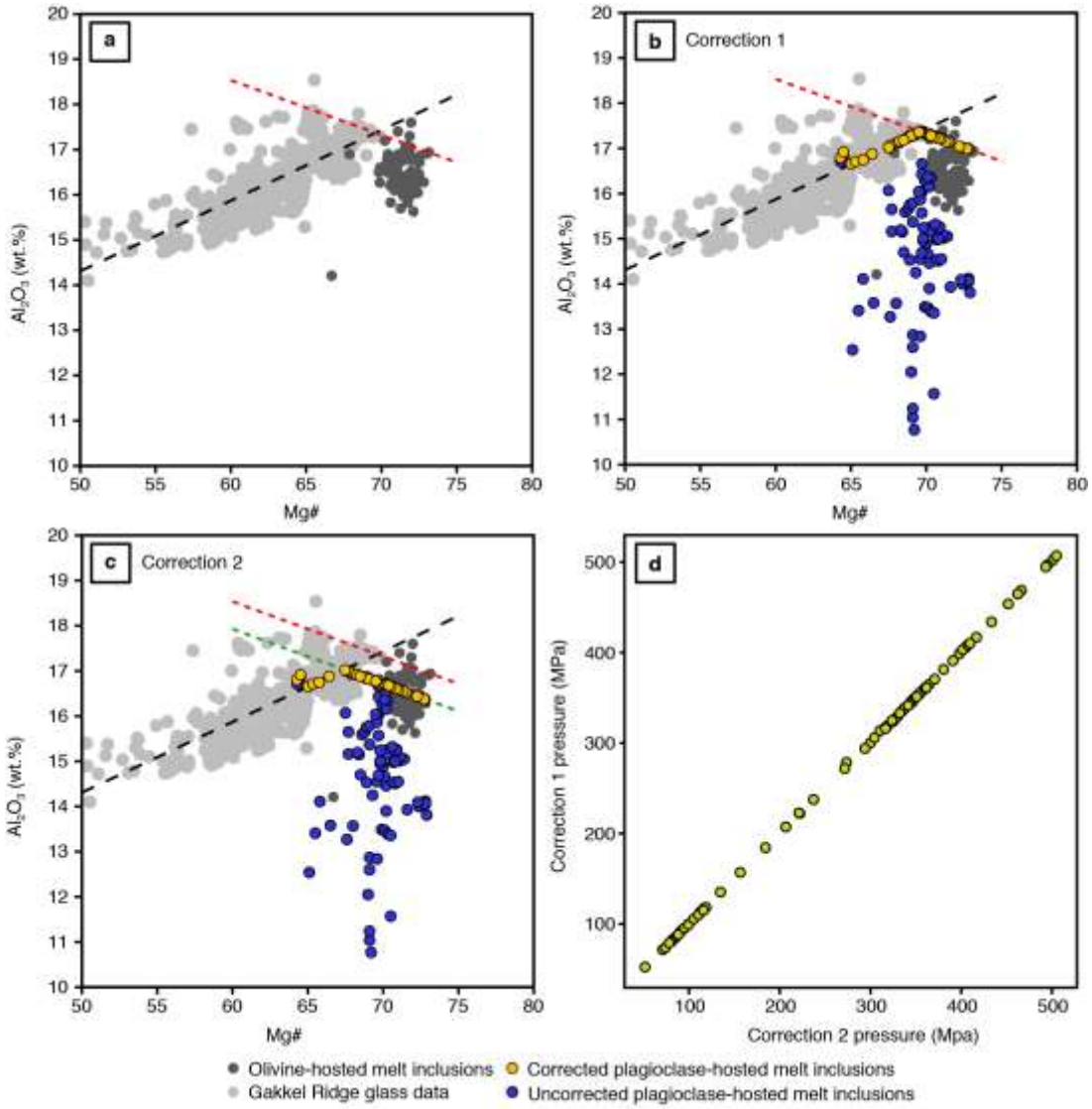

Extended Data Figure 7.

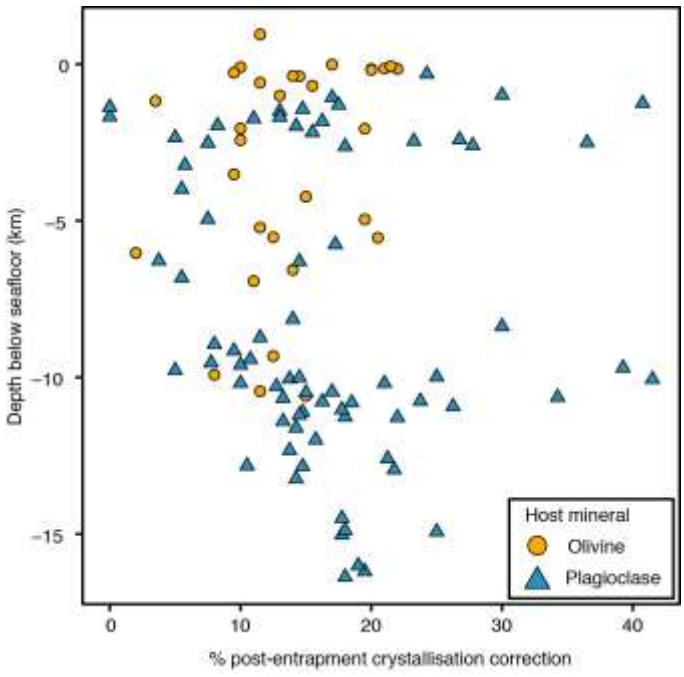

Extended Data Figure 8.

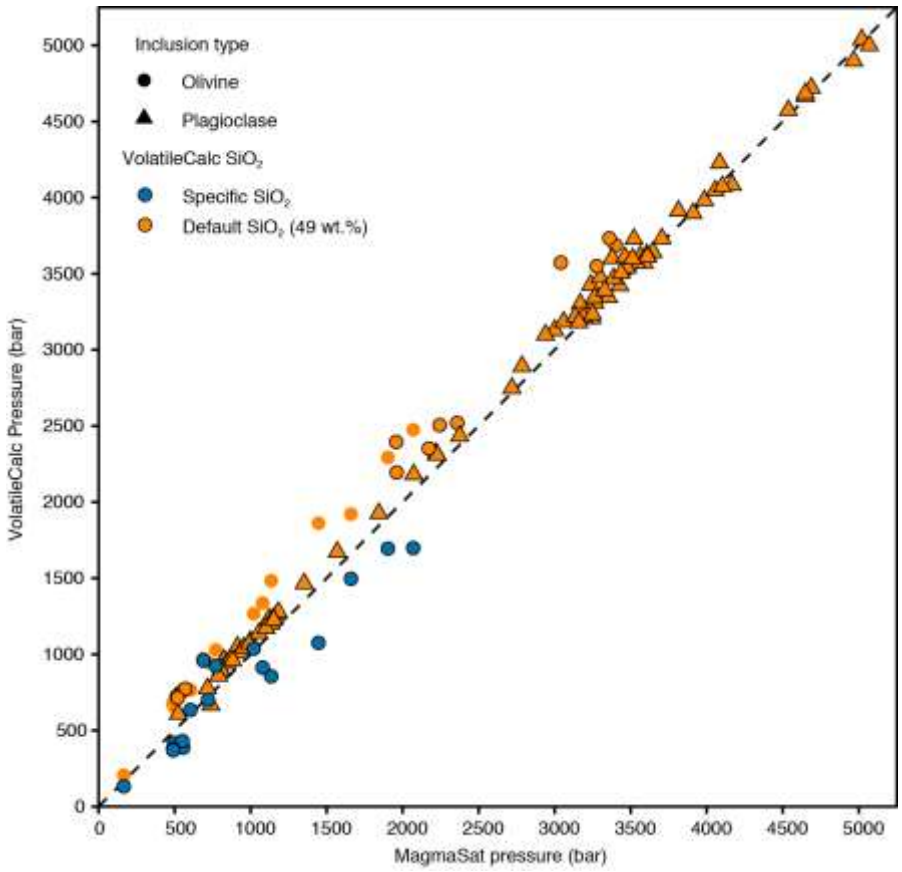

Extended Data Figure 9.